EDGE ARTICLE

Check for updates

All publication charges for this article have been paid for by the Royal Society of Chemistry

A core–brush 3D DNA nanostructure: the next generation of DNA nanomachine for ultrasensitive sensing and imaging of intracellular microRNA with rapid kinetics†

Lingqi Kong, Beibei Kou, Xiaolong Zhang, Ding Wang, Yali Yuan, [ID] Ying Zhuo, [ID] Yaqin Chai* and Ruo Yuan [ID] *

A highly loaded and integrated core–brush three-dimensional (3D) DNA nanostructure is constructed by programmatically assembling a locked DNA walking arm (DA) and hairpin substrate (HS) into a repetitive array along a well-designed DNA track generated by rolling circle amplification (RCA) and is applied as a 3D DNA nanomachine for rapid and sensitive intracellular microRNA (miRNA) imaging and sensing. Impressively, the homogeneous distribution of the DA and HS at a ratio of 1 : 3 on the DNA track provides a specific walking range for the DA to avoid invalid and random self-walking and notably improve the executive ability of the core–brush 3D DNA nanomachine, which easily solves the major technical challenges of traditional Au-based 3D DNA nanomachines: low loading capacity and low executive efficiency. As a proof of concept, the interaction of miRNA with the 3D DNA nanomachine could initiate the autonomous and progressive operation of the DA to cleave the HS for ultrasensitive ECL detection of target miRNA-21 with a detection limit as low as 3.57 aM and rapid imaging in living cells within 15 min. Therefore, the proposed core–brush 3D DNA nanomachine could not only provide convincing evidence for sensitive detection and rapid visual imaging of biomarkers with tiny change, but also assist researchers in investigating the formation mechanism of tumors, improving their recovery rates and reducing correlative complications. This strategy might enrich the method to design a new generation of 3D DNA nanomachine and promote the development of clinical diagnosis, targeted therapy and prognosis monitoring.

Introduction

In living systems, some highly complicated and hierarchical machines have evolved to perform significant biological processes with remarkable precision and efficiency.[1–3] Inspired by natural ingenuity, diverse DNA-based nanodevices have been created to convert chemical energy into mechanical motion,[4–8] holding great promise for intelligent drug delivery,[9–12] disease diagnosis[13–16] and biosensing analysis.[17–20] Recently, three-dimensional (3D) DNA nanomachines based on gold nano-particles (AuNPs)[21–24] have attracted extensive attention due to their improved abilities in simulating complex biological operation compared with one-dimensional (1D)[25,26] or two-dimensional (2D) DNA nanomachines.[27,28] However, the limited amount of track and the disordered immobilization of the DNA components (DNA walker and substrate) with

a heterogeneous nano (Au)-bio (DNA) interface resulted in the low loading capacity of DNA components and the invalid movement of the DNA walker, further restricting the whole executive ability and efficiency of the Au-based 3D DNA nano-machines. On account of these disadvantages, it has long been a challenging goal to develop a new type of 3D DNA nano-machine that could not only greatly enhance the loading capacity of the DNA components in an orderly manner, but also significantly improve the executive ability and efficiency.

Herein, a core–brush 3D DNA nanomachine with highly loaded and integrated properties was developed for intracel-lular microRNA (miRNA) imaging and ultrasensitive sensing with rapid kinetics (Scheme 1). Firstly, the extremely long DNA track cross-linked on a magnetic nanobead (MNB) was gener-ated by rolling circle amplification (RCA), in which the locked DNAzyme walking arm (DA) and electrochemiluminescent signal tag Rubpy (Ru) labeled hairpin substrate (HS) at a ratio of 1 : 3 were orderly assembled into the DNA track with a repetitive array to construct the core–brush 3D DNA nanomachine (PART A). According to PART B, once the target miRNA-21 was intro-duced into the 3D DNA nanomachine, the hybridization of
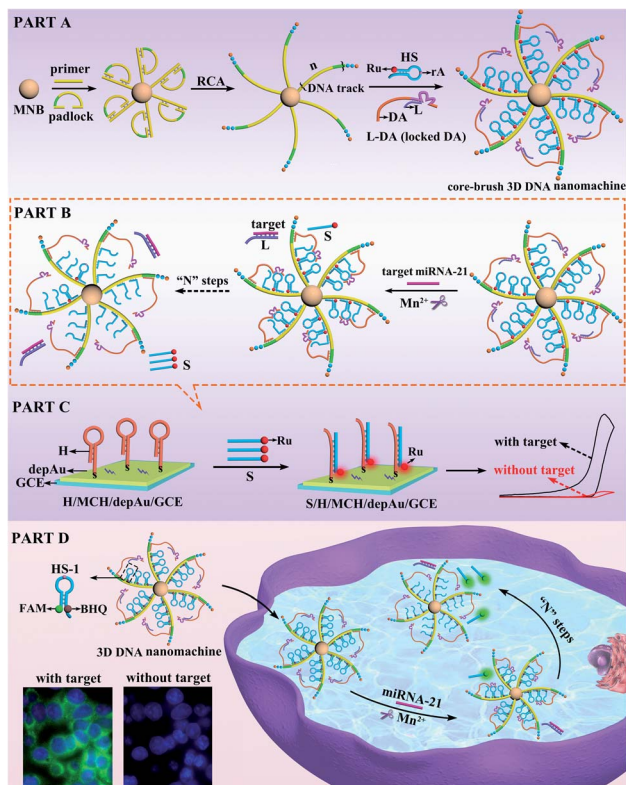
Scheme 1 Schematic illustration of the preparation of the core–brush 3D DNA nanomachine (part A) and target miRNA-21 induced recycle cleavage process (part B); The mechanisms of the ECL biosensing system for miRNA-21 sensitive detection (part C) and rapid intracellular imaging of miRNA-21 based on the core–brush 3D DNA nanomachine (part D).

miRNA-21 with a locking strand (L) *via* strand–displacement reaction could release the active DA from the locked DA (L-DA) to hybridize with the adjacent HS. Fueled by the DNAzyme-induced ribonucleotide hydrolysis, the HS was then cleaved by the active DA in the presence of cofactor Mn^{2+} to release the Ru-labelled segment (S). When S was captured by the DNA hairpin (H) onto a gold nanoparticle-assembled glassy carbon electrode (depAu/GCE) through the Au–S bond, a highly intense ECL signal was generated for ultrasensitive detection of miRNA-21 with a detection limit as low as 3.57 aM (PART C). Impressively, when the DA and HS-1 labelled with a fluorophore (FAM) and quencher (BHQ) were used to assemble our core–brush 3D DNA nanomachine (PART D), the intracellular miRNA-21 could activate autonomous motions of the DA to cleave the HS and release the FAM-labelled segment away from BHQ in the presence of the cofactor Mn^{2+}, leading to the quick fluorescence recovery of FAM within 15 min for sensitive imaging of low-abundance target miRNA-21. Compared with the limited amount of track in the Au-based 3D DNA nanomachine, the core–brush 3D DNA nanomachine not only provided a specific walking range for the DA to avoid inactive and stochastic self-walking, but also greatly increased the loading capacity and local concentrations of DNA components to significantly enhance the executive efficiency of the core–brush 3D DNA

nanomachine. Thus, this strategy gives impetus to exploit high-performance 3D DNA nanomachines for specific biological applications in complex cellular environments, such as bio-diagnostics and bioanalysis.

Results and discussion

Characterization analysis of the core–brush 3D DNA nanomachine

Polyacrylamide gel electrophoresis (PAGE) was employed to estimate the construction of the core–brush 3D DNA nano-machine. According to Fig. 1A, lane 1 and lane 2 displayed the primer and padlock. Then, a bright band with quite low mobility on the top of lane 3 suggested that a long DNA track was acquired successfully by a RCA reaction. Lane 4, lane 5, and lane 6 corresponded to the HS, L and DA, respectively. A bright single band of the L-DA was clearly observed in lane 7 with lower mobility, indicating that the DA could be effectively deactivated by L. A bright top band was observed in lane 8, which means that the L-DA and HS were successfully assembled onto the DNA track. The mixture of target miRNA-21 and L-DA represented two clear bands in lane 10. The lower band was the hybrid product of target miRNA-21 (lane 9) and L, implying that the hybridization of miRNA-21 with L could effectively release the DA from the L-DA *via* the strand–displacement reaction. Lane 11 and lane 12 illustrated the PAGE results for the proposed core–brush 3D DNA nanomachine with and without target miRNA-21. The bright band of abundant S was clearly observed
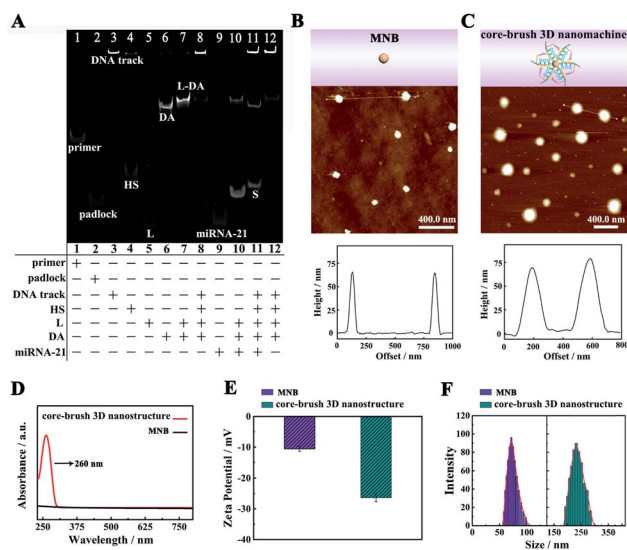
Fig. 1 (A) PAGE analysis of the core–brush 3D DNA nanomachine. Lane 1: primer; lane 2: padlock; lane 3: DNA track; lane 4: HS; lane 5: L; lane 6: DA; lane 7: L-DA; lane 8: DNA track + HS + L-DA; lane 9: miRNA-21; lane 10: L-DA + miRNA-21; lane 11 and lane 12 were the proposed assay with and without miRNA-21. AFM images of (B) the MNB core and (C) the core–brush 3D DNA nanomachine, respectively. Scale bars: 400 nm. (D) UV-vis absorption spectra, (E) zeta potential analysis and (F) hydrodynamic diameter distribution of the MNB core and core–brush 3D DNA nanomachine. Error bars represent the standard deviation of three experiments.

at the bottom band of lane 11, but not in lane 12, which demonstrated that miRNA-21 could active the proposed 3D DNA nanomachine to generate numerous S.

Then, we also employed atomic force microscopy (AFM), UV-vis spectroscopy, zeta potential analysis and dynamic light scattering (DLS) to verify the formation of the core–brush 3D DNA nanomachine. According to Fig. 1B and S1A,† the AFM characterization of the MNB core exhibited relatively smooth surfaces with a height of 66 nm approximately. After the accomplishment of the core–brush 3D DNA nanomachine, the apparent DNA brushes were observed on the surface of the core (Fig. 1C and S1B†) with an obvious increase in the height (70 nm). Likewise, the MNB core did not have any peak in the UV-vis absorption spectra (Fig. 1D, black line). Accompanied by the successful construction of the core–brush 3D DNA nanomachine, a very distinct characteristic deoxynucleotide absorption peak located at 260 nm was observed (Fig. 1D, red line). Moreover, the core–brush 3D DNA nanomachine possessed a decreased zeta potential of −26.41 mV compared with the MNB core of −10.57 mV owing to the negative charges of the DNA (Fig. 1E). As illustrated in Fig. 1F, the hydrodynamic diameter of the MNB core and core–brush 3D DNA nanomachine measured by DLS were around 68.5 nm and 233 nm, respectively. The hydrodynamic diameter of the core–brush 3D DNA nanomachine was bigger than the actual size owing to the formation of a hydrogen bond between the hydroxyl of H_2O and DNA. The remarkable comparisons of the above results suggested successful formation of the proposed core–brush 3D DNA nanomachine.

Execution efficiency of the designed core–brush 3D DNA nanomachine

To study the execution efficiency of the designed core–brush 3D DNA nanomachine (Fig. 2A) in contrast with the conventional 3D DNA nanomachine based gold nanoparticles (AuNPs) (Fig. 2B), we used fluorophore (FAM) and quencher (BHQ)-labeled HS-1 or FAM-labeled HS-2 to construct the proposed 3D DNA nanomachine and Au-based DNA nanomachine, respectively. In the presence of the cofactor Mn^{2+}, the target miRNA-21 could activate the DA to hybridize and cleave the HS for releasing the FAM-labelled segment (S) away from the quencher BHQ or AuNPs and obtaining the prominent fluorescence recovery of FAM. The real-time fluorescence of FAM for the proposed core–brush 3D DNA nanomachine showed a speedy fluorescence intensity growth and reached saturation about 900 s (Fig. 2C, curve a). In contrast, the typical Au-based 3D DNA nanomachine demonstrated a very slow fluorescence signal growth and the fluorescence saturation plateau did not appear within 2500 s (Fig. 2C, curve b). To calculate the initial rate of the DNA nanomachine, we verified the relationship between the fluorescence intensities and reaction time of the proposed 3D DNA nanomachine and the Au-based 3D DNA nanomachine. According to Fig. 3D, the fluorescence intensities shown the desirable linear relationships with the reaction time in the first 250 s. The regression equations of the proposed core–brush 3D DNA nanomachine (Fig. 2D, curve a and linear fit for curve a) and the Au-based 3D DNA nanomachine (Fig. 2D, curve b) were $I = 6.064t + 77.98$ and $I = 0.7522t + 311.3$, respectively. Based on the above results and related calculations, we found that the initial rate of our 3D DNA nanomachine (8.03×10^{-11} M s^{-1}) was more than 7-fold higher than that of the control Au-based 3D DNA nanomachine (1.11×10^{-11} M s^{-1}). Moreover, by first-order derivation of the real-time fluorescence increase curves of Fig. 2C, we could obtain the reaction rate curves of the DNA nanomachine as shown in Fig. 2E. The reaction rate of our designed 3D DNA nanomachine was extraordinarily high in the first 500 s and then became very low or even went to zero (Fig. 2E, curve a). In comparison, the reaction rate and the overall efficiency of the Au-based 3D DNA nanomachine were relatively low (Fig. 2E, curve b). Collectively,
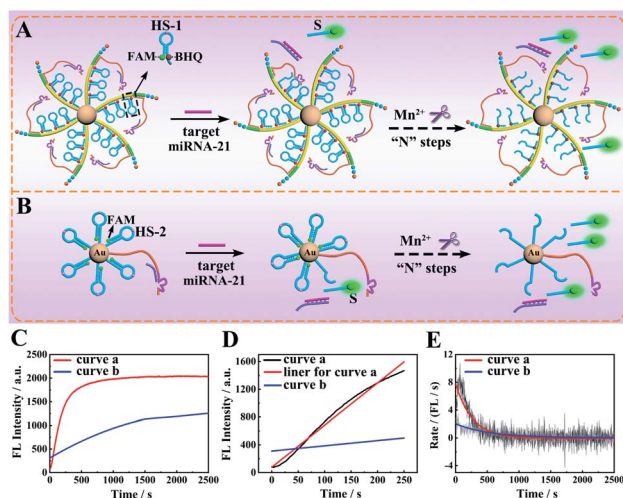

Fig. 2 Schematic illustration of operation of the proposed core–brush 3D DNA nanomachine (A) and the traditional Au-based 3D DNA nanomachine (B). Monitoring of the real-time fluorescence increase (C), initial moving rate (D) and reaction rate (E) of the proposed 3D DNA nanomachine and the Au-based 3D DNA nanomachine. Curves a and b in (C)–(E) represent the core–brush 3D DNA nanomachine and traditional Au-based 3D DNA nanomachine, respectively.
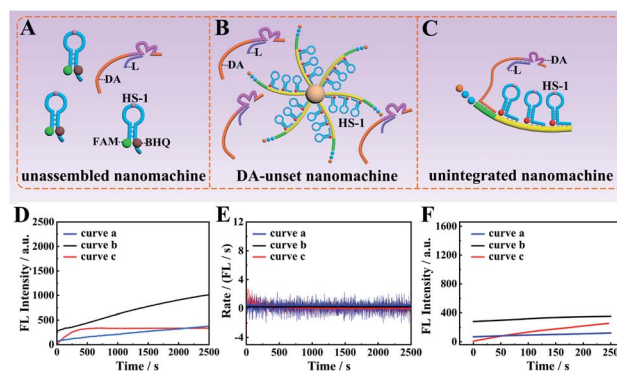

Fig. 3 Schematic illustration of the (A) unassembled nanomachine, (B) DA-unset nanomachine and (C) unintegrated nanomachine. (D) Real-time monitoring of fluorescence increase and (E) the reaction rate of these control nanomachines over a period of 2500 s. (F) Fluorescence changes of these control nanomachines in the first 250 s. Curve a–c in (D)–(F) represent the unassembled nanomachine, DA-unset nanomachine and unintegrated nanomachine, respectively.

these results demonstrated that the core–brush 3D DNA nanomachine possessed obviously higher execution efficiency than the Au-based 3D DNA nanomachine on account of the high loading and integration of the DNA components in an orderly manner on the programmable DNA track.

Feasibility investigation of the core–brush 3D DNA nanomachine

The core–brush 3D DNA nanomachine was composed of multiple components, and thus each component might have a potential impact on its overall executive efficiency. Firstly, we designed a control unassembled nanomachine that only contained a free DA and FAM and BHQ-labeled HS-1 at a ratio of 1 : 3 to confirm that the DA tended to walk along the HS-1 immobilized on the DNA track rather than the scattered HS-1 in the solution (Fig. 3A). Then, to verify that the highly executive efficiency of the proposed 3D DNA nanomachine was due to the ordered array of the DA and HS-1 on the programmed DNA track, the second control by mixing scattered DA with HS-1@MNB was designed to construct the DA-unset nanomachine in Fig. 3B. In this manner, the specific walking range for each DA was uncertain. Moreover, to ensure that the intense growth of fluorescence intensity was due to the highly loaded and integrated mode of our designed 3D DNA nanomachine, a control unintegrated nanomachine that only included a single DNA track assembled with a DA and HS-1 at 1 : 3 was further designed as shown in Fig. 3C. According to Fig. 3D, the fluorescence signal increase of the unassembled nanomachine (blue curve a) and the DA-unset nanomachine (black curve b) did not reach the saturation state in 2500 s. According to red curve c, although the unintegrated nanomachine reached reaction equilibrium quickly, its saturated fluorescence intensity was relatively weak. As depicted in Fig. 3E, the reaction rate of the unassembled nanomachine (curve a) and the DA-unset nanomachine (curve b) was extraordinarily low and even went to zero. Besides, the initial rate of the unintegrated nanomachine (8.60×10^{-11} M s^{-1}) was roughly close to that of our proposed 3D DNA nanomachine (Fig. 3F).

These results might be explained by effective collision theory that the reactants have to collide effectively with each other to make the reaction occur, and the concentrations of the reactants DA and HS-1 are proportional to the collision frequency. In the control unassembled nanomachine, the effective local concentrations of the DA and HS-1 were lower than that of being assembled together on the programmable DNA track, leading to low collision frequency and further decreasing the reaction efficiency. This result suggested that the programmable DNA track was a critical component to improve the effective local concentrations of reactants and further enhance the executive ability of the DNA walking nanomachine. Then, we thought that the chaotic reaction of scattered DA and HS-1 in the DA-unset nanomachine would reduce the utilization of DNA molecular components due to the uncertain walking range for each DA. In this manner, some DA-unset nanomachines might not hybridized with scattered DA, so these machines would not be in the operating state. Therefore, orderly assembling the DA and HS-1

into the programmable DNA track was the key to improving the utilization of DNA components. Furthermore, we also found that the saturated fluorescence intensity of the unintegrated nanomachine was weaker than that of our core–brush 3D DNA nanomachine. This result suggested that the highly integrated mode might greatly increase the effective local concentrations to further enhance the total fluorescence intensity. In principle, by comparing with the above control DNA nanomachines, our 3D DNA nanomachine possessed higher loading capacity and excellent executive efficiency, which gave impetus to ultrasensitive detection and rapid imaging of specific miRNA in cancer cells.

Application of the 3D DNA nanomachine for sensitive detection of miRNA-21

The proposed core–brush 3D DNA nanomachine was employed to construct an electrochemiluminescence (ECL) biosensing system for sensitive detection of miRNA-21. To verify the analytical performance of the sensing platform based on the proposed 3D DNA nanomachine, diverse concentrations of miRNA-21 were tested under the optimized experimental conditions (Fig. S2 and S3†). According to Fig. 4A, the ECL intensity gradually increased with incremental concentrations of miRNA-21 throughout the tested range (10 aM to 100 pM). As presented in Fig. 4B, the calibration plot demonstrated an excellent linear relationship between the ECL response and the logarithm of the miRNA-21 concentration. And its regression equation was $I = 1749.29 \lg c_{miRNA-21} + 6078.51$ with a correlation coefficient of 0.9990 and detection limit of 3.57 aM (S/N = 3). Moreover, compared with other methods for miRNA detection (Table S2†), the proposed strategy possessed a remarkably wider linear range and extremely lower detection limit, which manifested that the proposed core–brush 3D DNA
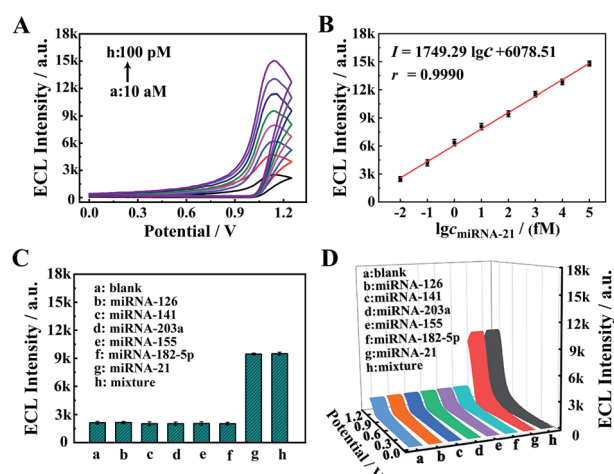

Fig. 4 (A) ECL intensities of the biosensor for target miRNA-21 at various concentrations. Curves a–h: 10 aM, 100 aM, 1 fM, 10 fM, 100 fM, 1 pM, 10 pM, and 100 pM. (B) Calibration plot of the ECL intensity and the logarithm of miRNA-21 concentrations. The detection limit was calculated in page S15. (C) The specificity and (D) corresponding ECL responses of the proposed biosensor toward target miRNA-21 (100 fM) against other miRNAs (each at 10 pM). Error bars: SD, n = 3.
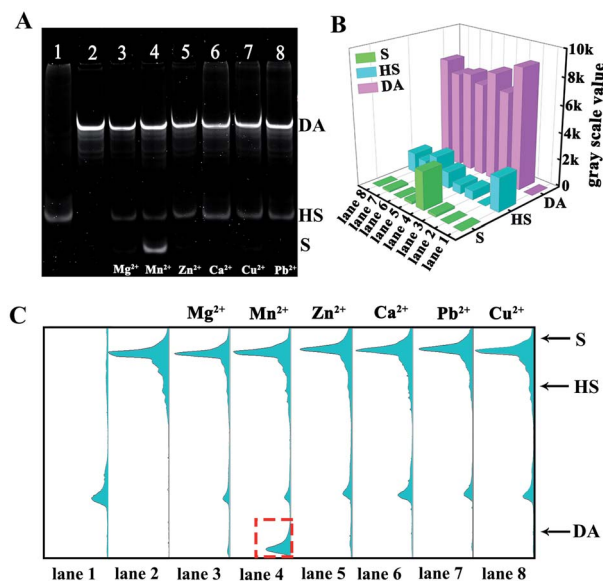
Fig. 5 (A) The specificity of the proposed strategy toward cofactor Mn^{2+} (15 mM) against other cofactors (each at 150 mM). The quantitative gray scale value (B) and the total gray scale analysis (C) of part A.

Fig. 6 MCF-7 cells cultured with (A) the proposed core−brush structured 3D DNA nanomachine and (B) the conventional Au-based walking nanomachine in the presence of cofactor Mn^{2+}. HeLa cells cultured with (C) the proposed 3D DNA nanomachine and (D) the conventional Au-based walking nanomachine in the presence of cofactor Mn^{2+}. The length of the scale bar is 20 μm.

nanomachine has potential applications in ultrasensitive biomarker detection and metrology.

To validate the specificity of our proposed 3D DNA nanomachine for sensitive detection of miRNA-21, a series of interfering agents containing miRNA-126, miRNA-141, miRNA-203a, miRNA-155 and miRNA-182-5p were introduced as interference tests. According to Fig. 4C and D, the ECL intensity of interfering agents (10 pM) was almost negligible as the blank one. In contrast, the mixture containing target miRNA-21 was similar to that of miRNA-21 (100 fM), exhibiting an obvious ECL intensity. Meanwhile, the proposed biosensor also showed excellent selectivity for mismatched miRNA-21 (Fig. S7†). Next, the selectivity of our strategy based on Mn^{2+}-dependent DNAzyme was also monitored by PAGE. As demonstrated in Fig. 5A, lane 1 represents the HS, lane 2 represents the DA, and lanes 3–8 represent the cleavage of the HS by the DA in the presence of Mg^{2+}, Mn^{2+}, Zn^{2+}, Ca^{2+}, Cu^{2+} and Pb^{2+} as alternative cofactors, respectively. As expected, the most obvious band of cleavage products (S) appeared in lane 4, indicating that Mn^{2+} was the best cofactor to truncate S from the DA. The above results clearly demonstrate the high selectivity of our proposed 3D DNA nanomachine. Meanwhile, the gray scale intensity of the PAGE bands was analyzed by Image J. The highest gray scale value of S and the most obvious band of S were observed in lane 4 of Fig. 5B and C with the cofactor Mn^{2+}, which were consistent with the results of gel electrophoresis. Furthermore, the proposed biosensing platform also presented outstanding stability and repeatability selectivity (Fig. S8†).

Rapid and sensitive imaging of miRNA-21 in living cells

At first, endocytosis inhibition experiments and MTT assays were implemented to reveal the uptake mechanism of our nanomachine (Fig. S9†) and demonstrate the low cytotoxicity of
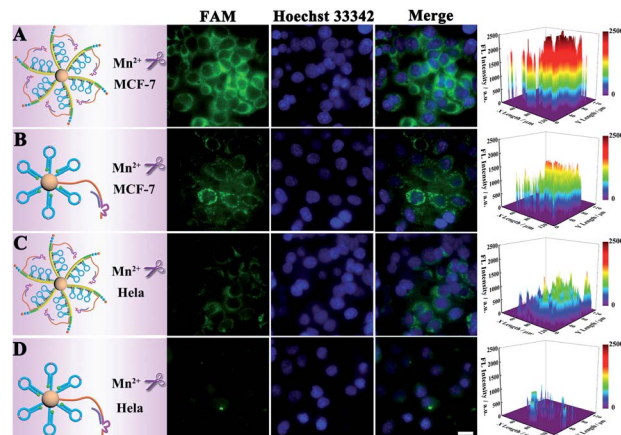
our strategy (Fig. S10†), respectively. Then, MCF-7 cells and HeLa cells were used to evaluate the imaging ability of the developed core–brush 3D DNA nanomachine for intracellular miRNA-21. As presented in Fig. 6A, MCF-7 cells, with high miRNA-21 expression, showed remarkably strong fluorescence with the cultivation of the core–brush 3D DNA nanomachine. Meanwhile, fluorescence that was obviously distinguishable from the background could be observed inside HeLa cells with a low miRNA-21 expression level (Fig. 6C). By contrast, the intracellular fluorescence intensity of MCF-7 cells cultured with the conventional Au-based 3D DNA nanomachine was distinctly weaker than that of with the proposed 3D DNA nanomachine (Fig. 6B). Especially for HeLa cells, only a low intracellular fluorescence intensity was noticed with the cultivation of the traditional Au-based 3D DNA nanomachine (Fig. 6D). Thus, compared with the conventional Au-based 3D DNA nanomachine, the proposed core–brush 3D DNA nanomachine could
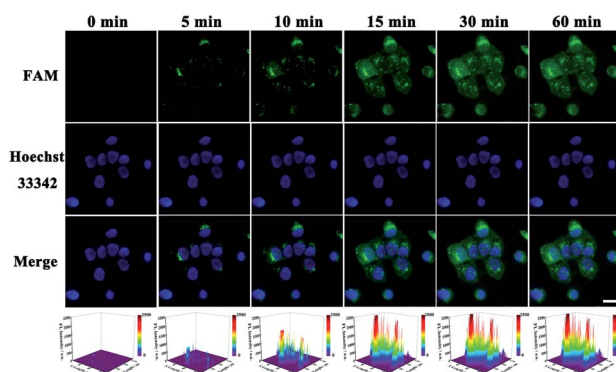

Fig. 7 Real-time imaging of MCF-7 cells cultured with the proposed core−brush 3D DNA nanomachine within 60 min. 0 min refers to the time point when Mn^{2+} was added into the operating buffer. The length of the scale bar is 20 μm.

Table 1 Comparison of the needed time for our method and other methods for miRNA imaging

Method	Detection target	Saturation time	Ref.
Integrated smart nanodevice	miRNA-21	300 min	29
ATP-powered DNA nanomachine	miRNA-21	80 min	30
Au NR dimer-UCNP core–satellite nanostructures	miRNA-21	480 min	31
MicroRNA-initiated DNAzyme motor	miRNA-10b	60 min	22
Entropy-driven DNA nanomachine	miRNA-21	300 min	32
Enzyme-free molecular catalytic device	miRNA-155	240 min	33
Core–brush 3D DNA nanomachine	miRNA-21	15 min	This work

not only make it possible to image low-expressed miRNA-21 with higher sensitivity, but also offer a general strategy for accurate imaging in living cells with higher specificity. Moreover, we also used the miRNA-21 mimic and inhibitor to further verify the specific discrimination of intracellular miRNA-21 by the core–brush 3D DNA nanomachine (Fig. S11†). We believe that the proposed core–brush 3D DNA nanomachine could provide an attractive way for sensitive imaging of intracellular specific miRNA in low abundance, which could contribute to study the biological processes and mechanisms within the cell system and its application in early diagnosis and treatment of diseases.

Furthermore, real-time imaging of MCF-7 cells cultured with the proposed 3D DNA nanomachine at different incubation time points within 60 min is tracked in Fig. 7. Impressively, the brightest fluorescence was observed in about 15 min and no obvious fluorescence growth was noticed within 60 min, indicating that the visualization of intracellular miRNA-21 was achieved within 15 min with the proposed core–brush 3D DNA nanomachine, which was noticeably faster than those of previously reported nanomachines (Table 1). These results confirmed that the rapid imaging strategy based on the proposed 3D DNA nanomachine might offer great potential for rapid point-of-care medical devices and early detection of cancer in clinical practices.

Conclusions

In summary, we presented a core–brush 3D DNA nanomachine by innovatively assembling DNA components (DA and HS) into a repetitive array on a programmable DNA track. Compared with traditional Au-based 3D DNA nanomachines, our strategy had the following combined advantages. First, the DNA track generated by a RCA reaction was well-designed to homogeneously arrange DNA components, which not only ensured a specific walking range for the DA to prevent stochastic and invalid movement, but also avoided the discorded nano-bio interface of Au/DNA in the Au-based 3D DNA nanomachine. Second, the highly integrated 3D DNA nanomachine possessed an enhanced loading capacity and movement efficiency due to the organized and high local concentration of DNA components. Third, as practical applications, the proposed 3D DNA nanomachine was successfully applied for rapid and sensitive detection and imaging of intracellular specific miRNA, which

could help us explore its biological functions in tumor differentiation and proliferation as well as potential drug screening in early disease diagnosis.

Data availability

The data that support the findings of this study are available in the ESI.†

Author contributions

L. K. and R. Y. developed the concept and design of the project. L. K. performed experiments. All authors contributed to the analysis and the interpretation of the results. The manuscript was written by L. K. and revised by Y. C. and R. Y. All authors have given approval for the final version of the manuscript.

Conflicts of interest

There are no conflicts to declare.

Acknowledgements

References

1 A. G. Tsai, D. R. Glass, M. Juntilla, F. J. Hartmann, J. S. Oak, S. Fernandez-Pol, R. S. Ohgami and S. C. Bendall, *Nat. Med.*, 2020, **26**, 408–417.
2 A. J. Thubagere, W. Li, R. F. Johnson, Z. Chen, S. Doroudi, Y. L. Lee, G. Izatt, S. Wittman, N. Srinivas, D. Woods, E. Winfree and L. Qian, *Science*, 2017, **357**, eaan6558.
3 C. Jung, P. B. Allen and A. D. Ellington, *Nat. Nanotechnol.*, 2016, **11**, 157–163.
4 E. Kopperger, J. List, S. Madhira, F. Rothfischer, D. C. Lamb and F. C. Simmel, *Science*, 2018, **359**, 296.
5 Q. Li, L. Liu, D. Mao, Y. Yu, W. Li, X. Zhao and C. Mao, *J. Am. Chem. Soc.*, 2020, **142**, 665–668.
6 J. Valero, N. Pal, S. Dhakal, N. G. Walter and M. Famulok, *Nat. Nanotechnol.*, 2018, **13**, 496–503.

7 J. Chao, J. Wang, F. X. Ouyang, E. Kopperger, H. Liu, Q. Li, J. Shi, L. Wang and J. Hu, *Nat. Mater.*, 2019, **18**, 273–279.

8 C. Ouyang, S. Zhang, C. Xue, X. Yu, H. Xu, Z. Wang, Y. Lu and Z. S. Wu, *J. Am. Chem. Soc.*, 2020, **142**, 1265–1277.

9 Y. Zhang, X. B. Zhang, Y. Y. Li, Y. L. He, Y. Liu and H. X. Ju, *Chem. Sci.*, 2020, **11**, 6289–6296.

10 C. Xue, S. X. Zhang, C. H. Ouyang, D. Chang, B. J. Salena, Y. F. Li and Z. S. Wu, *Angew. Chem., Int. Ed.*, 2018, **57**, 9739–9743.

11 J. Jiang, P. Zhang, Y. M. Nie, K. F. Peng, Y. Zhuo, Y. Q. Chai and R. Yuan, *Chem. Sci.*, 2020, **11**, 2193–2199.

12 S. Zhang, C. Chen, C. Xue, D. Chang, H. Xu, B. J. Salena, Y. Li and Z. S. Wu, *Angew. Chem., Int. Ed.*, 2020, **59**, 14584–14592.

13 J. Zhang, M. He, C. Nie, M. He, Q. Pan, C. Liu, Y. Hu, T. Chen and X. Chu, *Chem. Sci.*, 2020, **11**, 7092–7101.

14 M. Raveendran, A. J. Lee, R. Sharma, C. Wälti and P. Actis, *Nat. Commun.*, 2020, **11**, 4384.

15 S. Yue, X. Song, W. Song and S. Bi, *Chem. Sci.*, 2019, **10**, 1651–1658.

16 J. Zhao, H. Chu, Y. Zhao, Y. Lu and L. Li, *J. Am. Chem. Soc.*, 2019, **141**, 7056–7706.

17 H. Zhang, X. Xu and W. Jiang, *Chem. Sci.*, 2020, **11**, 7415–7423.

18 Z. Zhou, J. D. Brennan and Y. Li, *Angew. Chem., Int. Ed.*, 2020, **59**, 10401–10405.

19 P. Zhang, J. Jiang, R. Yuan, Y. Zhuo and Y. Q. Chai, *J. Am. Chem. Soc.*, 2018, **140**, 9361–9364.

20 M. S. Xiao, K. Zou, L. Li, L. H. Wang, Y. Tian, C. H. Fan and H. Pei, *Angew. Chem., Int. Ed.*, 2019, **58**, 15448–15454.

21 M. M. Lv, J. W. Liu, R. Yu and J. H. Jiang, *Chem. Sci.*, 2020, **11**, 10361–10366.

22 H. Peng, X. F. Li, H. Zhang and X. C. Le, *Nat. Commun.*, 2017, **8**, 14378.

23 P. Q. Ma, Q. Huang, H. D. Li, B. C. Yin and B. C. Ye, *J. Am. Chem. Soc.*, 2020, **142**, 3851–3861.

24 Y. Li, G. A. Wang, S. D. Mason, X. Yang, Z. Yu, Y. Tang and F. Li, *Chem. Sci.*, 2018, **9**, 6434–6439.

25 P. K. Lat, C. W. Schultz, H. Z. Yu and D. Sen, *Angew. Chem., Int. Ed.*, 2021, **60**, 8722–8727.

26 Q. Wei, J. Huang, J. Li, J. Wang, X. Yang, J. Liu and K. Wang, *Chem. Sci.*, 2018, **9**, 7802–7808.

27 T. E. Tomov, R. Tsukanov, Y. Glick, Y. Berger, M. Liber, D. Avrahami, D. Gerber and E. Nir, *ACS Nano*, 2017, **11**, 400.

28 J. Valero and M. Famulok, *Angew. Chem., Int. Ed.*, 2020, **59**, 16366–16370.

29 P. He, W. Han, C. Bi, W. Song, S. Niu, H. Zhou and X. Zhang, *ACS Nano*, 2021, **15**, 6961–6976.

30 P. Q. Ma, C. P. Liang, H. H. Zhang, B. C. Yin and B. C. Ye, *Chem. Sci.*, 2018, **9**, 3299–3304.

31 W. Ma, P. Fu, M. Sun, L. Xu, H. Kuang and C. Xu, *J. Am. Chem. Soc.*, 2017, **139**, 11752–11759.

32 C. P. Liang, P. Q. Ma, H. Liu, X. G. Guo, B. Yin and B. C. Ye, *Angew. Chem., Int. Ed.*, 2017, **56**, 9077.

33 S. Yue, X. Song, W. Song and S. Bi, *Chem. Sci.*, 2019, **10**, 1651–1658.